

Design and Fabrication of Kidney Phantoms for Internal Radiation Dosimetry using 3D Printing Technology

Author Names and Degrees:

Dr. Johannes Tran-Gia^{1*}

Susanne Schlögl¹

Prof. Dr. Michael Lassmann¹

Affiliations:

¹ Department of Nuclear Medicine, University of Würzburg, Würzburg, Germany

***Correspondence to:**

Johannes Tran-Gia

Department of Nuclear Medicine

University of Würzburg

Oberdürrbacher Str. 6

97080 Würzburg, Germany

Phone: +49-931-201-35421

Email: Tran_J@ukw.de

Running Title:

3D-Printed Kidney Phantoms for Dosimetry

Word Count:

This manuscript contains 5577 words.

ABSTRACT

Currently, the validation of multimodal quantitative imaging and absorbed dose measurement is impeded by the lack of suitable, commercially available anthropomorphic phantoms of variable sizes and shapes. To demonstrate the potential of 3D printing techniques for quantitative SPECT/CT imaging, a set of kidney dosimetry phantoms and their spherical counterparts was designed and manufactured with a fused deposition modeling 3D printer. Nuclide-dependent SPECT/CT calibration factors were determined to assess the accuracy of quantitative imaging for internal renal dosimetry.

Methods

A set of four one-compartment kidney phantoms with filling volumes between 8 mL and 123 mL was designed based on the outer kidney dimensions provided by MIRD Pamphlet 19. After printing the phantoms, SPECT/CT acquisitions of three radionuclides (Tc-99m, Lu-177, and I-131) were performed and calibration constants determined for each radionuclide-volume combination. A set of additionally manufactured spheres matching the kidney volumes was additionally examined to assess the influence of the phantom shape and size on the calibration constants.

Results

A set of refillable, waterproof and chemically stable kidneys and spheres was successfully manufactured. Average calibration factors for Tc-99m, Lu-177, and I-131 were obtained in a large source measured in air. For the largest phantom (122.9 mL), the VOIs had to be enlarged by 1.2 mm (Tc-99m), 2.5 mm (Lu-177), and 4.9 mm (I-131) in all directions to obtain calibration factors comparable to the reference. While partial-volume effects were observed for decreasing

phantom volumes (percentage difference up to 9.8% for the smallest volume of 8.6 mL), the difference between corresponding sphere/kidney pairs was small ($< 1.1\%$ for all volumes).

Conclusion

3D printing is a promising prototyping technique for geometry-specific calibration of SPECT/CT systems. While the underlying radionuclide and the related collimator have a major influence on the calibration, no relevant differences between kidney-shaped and spherically-shaped uniform-activity phantoms were observed. With comparably low costs and sub-mm resolution, 3D printing techniques hold the potential for manufacturing individualized anthropomorphic phantoms in many clinical applications in Nuclear Medicine.

Key Words:

Anthropomorphic Phantom Design (Kidney), 3D Printing, Internal Radiation Dosimetry, Quantitative SPECT Imaging, Gamma Camera Calibration

INTRODUCTION

The kidneys represent the critical organ in many radionuclide therapies involving peptides or small molecules (1-4). An important prerequisite for a reliable dosimetry based on planar and SPECT/CT images are measurements on quasi-realistic anthropomorphic phantoms of a known activity concentration (5-7). However, industrial manufacturing of such phantoms is expensive and only profitable for the production of larger quantities. Therefore, only few phantoms representing very rough approximations of the underlying anatomies – in most cases an arrangement of simple geometrical objects such as spheres and cylinders – are commercially available, impeding a validation of quantitative imaging and the related absorbed dose estimation based on patient- or even only organ-specific geometries.

After the introduction of stereolithography more than two decades ago (8), a wide range of rapid prototyping technologies (9) have evolved. More recently, some of these techniques have become commercially available under the term “3D printing” (10,11), enabling an individual production of phantoms with more customized geometries, and therefore offering an attractive alternative to industrial phantom construction. The majority of 3D printing setups recently proposed for phantom design are based on stereolithography (12,13) or polyjet/multijet techniques (14-16). While these photopolymerization-based 3D printing techniques feature the highest resolution that is currently commercially available (as low as ~ 20 microns), high investment costs in the six-digit USD range limit their application area to financially well-endowed research centers or commercial and therefore non-individualized production.

To hold out the prospect for a widespread use of 3D printing in clinical applications such as internal radiation dosimetry, the potential of the considerably more affordable fused deposition modeling (FDM) 3D printing technique (initial costs in the four-digit USD range) for

manufacturing anthropomorphic phantoms was sounded out in this work. To assess the effect of the phantom geometry on quantitative SPECT/CT imaging, a set of kidney phantoms was designed based on MIRD pamphlet 19 (17) and fabricated using an FDM-based 3D printer. Additionally, a set of volumetrically corresponding spheres, as they are typically used for SPECT calibration, was produced. Finally, SPECT/CT acquisitions of all combinations of radionuclides and age-models were performed with different radionuclides (Tc-99m, Lu-177, I-131) to assess geometrical effects as well as radionuclide/collimator dependence on the calibration constants obtained in a volume-of-interest (VOI) analysis.

METHODS

Design of a Kidney Model Following MIRD Pamphlet 19

Simplified versions of four of the six age-dependent kidneys described in (17) with volumes between 8 mL and 123 mL were used as kidney models in this work. The renal cortex is characterized by an ellipsoid with two half-axes of approximately the same size (a_{MIRD19} , c_{MIRD19}) as well as one shorter half-axis (b_{MIRD19}). A plane perpendicular to one of the longer half-axes represents the renal pelvis. To simplify the model and thereby the demand on the 3D printer, representations of the medullary pyramids were omitted in this work, reducing the initial multi-compartment kidney to a one-compartment model. To additionally reduce the complexity of the computational 3D modeling, the ellipsoidal basic shape of the kidney was turned into a spheroid by averaging the two longer half-axes ($a_{\text{new}} = c_{\text{new}} > b_{\text{new}}$). The cut resembling the renal pelvis was performed at a distance d_{pelvis} from the origin. The MIRD19 and the adapted kidney dimensions are given in the top part of Table 1.

Computational Modeling of the Kidney Model

Computer aided designs (CADs) of the kidney models presented in the previous paragraph were created in Autodesk Inventor Professional 2016 (Autodesk, San Rafael, CA) using basic drawing commands (extrude, revolve, thicken, fillet). A wall thickness of 1.2 mm was used to make the phantoms sufficiently rigid while keeping the amount of employed filament to a minimum. All CAD models are depicted in Figure 1. To enable the filling of the phantom, a cylinder of 17 mm height as well as 6 mm diameter was added opposite to the renal pelvis (green arrow in Figure 1a). Two cylinders of 6 mm diameter were added at two opposite sides of each kidney model

(red arrows in Figure 1a) to fix the phantom in the PET body phantom L981602 (PTW-Freiburg, Freiburg, Germany). The completed CAD models were exported in the stereolithography (STL) interface format.

In addition, four spheres matching the respective kidney volumes were constructed to validate the kidney phantoms against the spherical geometry typically used for calibration of SPECT/CT systems. After extracting the kidney fill volumes (V_K) using the Autodesk Inventor iProperties function, the radii (r_s) of the reference spheres were calculated according to $V_K \approx V_S = \frac{4}{3}\pi r_s^3$. Based on these radii, spheres were modeled in Autodesk Inventor using basic drawing commands (depicted in Supplemental Figure 1). All fill volumes and radii are given in the bottom part of Table 1.

Slicing & 3D Printing the Models

3D printing was performed using a Renkforce RF1000 3D printer (Conrad Electronic, Hirschau, Germany) which works by fusion deposition modeling (FDM). In this technique, a plastic filament is heated by an extrusion nozzle (red arrow in Figure 2a). The melted material is extruded onto a movable printing plate (red arrow in Figure 2b). As the filament hardens immediately after extrusion from the nozzle, an entire 3D object can be created by laying down successive layers of material. In this work, Voltivo ExcelFil transparent polylactic acid (PLA) with a thickness of 3 mm was used as filament (Voltivo Group, Taipei, Taiwan). According to (18), Hounsfield units of these filaments lie in the range of 100-200.

The printer was controlled through a PC using Repetier-Host V1.5.0 (Hot-World, Willich, Germany). An embedded slicing software (Slic3r 1.2.9) takes the imported STL model and combines it with all necessary printing parameters (e.g. layer height, extrusion thickness, and

number of perimeters per layer) to create the machine-readable G-code required for printing each layer. Supplemental Figure 2 shows an example for the slicing of the adult kidney (a) and the corresponding sphere (b).

As it is impossible to print overhangs or other horizontal object parts without an underlying structure (such as the upper half of the spheres in Supplemental Figure 1), support material, which is printed with lower fill density, and which is only loosely attached to the main object, is added in the slicing procedure (red arrows in Supplemental Figure 2). To enable the retrospective removal of support material, each kidney was separated into renal pelvis and renal cortex (Supplemental Figure 2a shows part of the sliced cortex without the pelvis). Similarly, the spheres had to be separated in two halves (Supplemental Figure 2b). Images of the 3D printing procedure of the renal pelvis are shown in Figure 2.

After the print, the support material was removed and the different components were agglutinated using a two component epoxy adhesive of medium viscosity (LOCTITE EA 3430, Henkel, Düsseldorf, Germany). Subsequently, a filling hole of M1.2 was drilled into the filling cylinder, which was widened to M3.0 in the top half to make it sealable with a plastic screw and O-ring. Additionally, M6.0 thread profiles were cut at the ends of the attachment cylinders. Finally, the phantoms were coated with a low-viscosity epoxy casting resin (E300GB, Breddermann Kunstharze, Schapen, Germany) to ensure water tightness and chemical stability against the typically alkaline isotope solutions. A picture of the final set of phantoms is given in Figure 3.

Attachment System for the Body Phantom

An attachment system for the PET body phantom was printed to ensure an easy insertion and removal of the kidney/spherical inserts. The associated CAD model is shown in Figure 4a. It includes three holes (width M6.0) for height adjustment of the kidney inserts within the body phantom (red arrows in Figure 4a). Additionally, it contains four screw holes (width M4.0) for the insertion of spacers, fixing the attachment system to the body phantom's lid (green arrows in Figure 4a). 3D printing was performed using the same setup and parameters as described above. The attachment of the kidney insert is shown in Figure 4b: After screwing the kidney insert into the bottom of the body phantom (blue arrow), two screw nuts (M6.0) are used to mount the attachment system (green arrows). Finally, the four spacers are adjusted to fix the position of the lid (green boxes) before the phantom is closed.

Determination of the Filling Weight

Prior to the measurements, all phantoms were weighed with a Kern PCB 3500-2 precision mass scale (Kern & Sohn, Balingen-Frommern, Germany) with a readability of 0.01 g. Subsequently, they were filled with water and weighed again to determine the filling volumes and additionally assure water tightness.

Preparation of the Phantom

In each experiment, one of the kidneys or spherical phantoms and a 100 mL plastic bottle were filled with a homogenous isotope solution of a desired specific activity, a_{spec} . The isotope solution was produced by dissolving a highly-concentrated radionuclide solution of a known activity, A_{total} , in a non-radioactive liquid. The activity A_{total} was determined using a VDC-405 dose calibrator with a VIK-202 ionization chamber (Comcer, Joure, Netherlands), which had

previously been cross-calibrated to a high-purity germanium detector (HPGE, Canberra, Meriden, CT) whose energy-dependent efficiency was calibrated with several NIST-traceable standards over the energy range considered. While Tc-99m was combined with water, Lu-177 and I-131 were combined with 0.1M HCl and 1M NaOH respectively, to keep the ions dissolved. After adding the activity to the liquid, the total weight w_{solution} of the solution was obtained using the precision scale (difference filled minus empty container). After measuring the activity A_{back} remaining in the syringe, the specific activity was calculated as:

$$a_{\text{spec}}(t_{\text{ref}}) = \frac{A_{\text{total}}(t_{\text{ref}}) - A_{\text{back}}(t_{\text{ref}})}{w_{\text{solution}}} . \quad (1)$$

For consistency, all activities were recalculated to a reference time t_{ref} – typically the time of the initial activity measurement. After filling the kidney/sphere and the plastic bottle with the isotope solution, the kidney/sphere was attached to the body phantom, the rest of which was filled with water to emulate soft tissue. The plastic bottle was placed next to the phantom as reference. As there is no attenuation from surrounding materials such as Lucite or water, this reference bottle will be called “attenuation-free reference” in what follows.

SPECT/CT Acquisition

SPECT/CT acquisitions of this setup were performed using a Siemens Symbia T2 system (Siemens Healthcare, Erlangen, Germany) with a 15.9 mm thick crystal.

First, SPECT images were acquired (auto-contouring, detector configuration: 180°, pixel size: 4.8×4.8 mm², matrix size: 128×128, acquisition time: 30 min, 60 views). The collimators were chosen according to the isotope used in the respective acquisition (Tc-99m: LEHR, Lu-177: MELP, I-131: high-energy). Subsequent to the SPECT acquisition, CT images were acquired

(mAs: 17, kVp: 130, slice thickness: 5.0 mm, field-of-view: 500×500 mm², matrix size: 512×512).

SPECT images were reconstructed with the OSEM iterative reconstruction algorithm and a collimator depth-dependent three-dimensional resolution recovery (Flash 3D, 6 subsets, 6 iterations, no filtering). Attenuation correction was performed based on the CT μ -maps. Scatter correction was performed using a double-energy (Tc-99m) or triple-energy window method (Lu-177 & I-131). The energy windows for the main emission photo peak and the adjacent lower and upper scatter energy windows are defined in Table 2.

Finally, CT acquisitions of an additionally printed 15×15×15 mm³ PLA cube were made to determine the Hounsfield unit of the PLA filament.

Determination of the Calibration Factor

Calibration factors were determined as follows: CT-based VOIs were drawn using the provided software tool (Syngo MI Applications, VA60C). While ellipsoids with the theoretically known dimensions were used in case of the spherical phantoms, layer-by-layer polygons were drawn for the more irregular shapes of the kidney and the reference bottle. Based on these VOIs, calibration factors (CF) were calculated by dividing the total number of counts (n_{counts}) by the activity at the start of the acquisition (A_{start}) and the duration of the acquisition (d_{acq}): $CF = n_{counts}/A_{start}/d_{acq}$.

To compensate for spill-out effects caused by the limited resolution of the imaging system, the volumes of all VOIs were extended by an isotope-dependent VOI enlargement factor $\Delta\rho$ in all directions. It was determined separately for each isotope by matching the calibration factor of the largest sphere to the calibration factor of the associated reference bottle. By comparing the radius

of the corresponding sphere to the nominal radius, $\Delta\rho$ – defined as a multiple of the pixel size px – was determined (e.g. $\Delta\rho = 0.5px$ for an enlargement by 2.4 mm for pixel size $px = 4.8$ mm). This factor was subsequently applied to all other acquisitions of the associated isotope. All calibration factors given in this work were obtained using the enlarged VOIs.

RESULTS

Accuracy of the 3D Printing Technique

Supplemental Table 1 shows the theoretical as well as the measured filling volumes of all phantoms. To simplify the conversion, *unit density* was assumed.

The error between the filling volumes of the CAD design and the actual 3D print increases with decreasing dimensions of the object (adult kidney/sphere: 2.4%/0.5%, newborn kidney/sphere: 5.8%/1.2%). Additionally, the error is considerably smaller for the spherical phantoms (maximum error of 1.2% for the smallest volume).

SPECT/CT Acquisition & Reconstruction

An average Hounsfield unit of ~ 142 was observed in the CT acquisition of the PLA cube.

The average specific activities used for the calibration measurements were (0.90 ± 0.06) MBq/mL for Tc-99m, (0.99 ± 0.05) MBq/mL for Lu-177, and (0.26 ± 0.01) MBq/mL for I-131.

It should be noted that, in this case, the standard deviation describes the variation in specific activity between subsequent SPECT/CT acquisitions. These differences can be caused by radioactive decay of the isotope solution between subsequent SPECT/CT acquisitions (especially for Tc-99m with the shortest half-life), but they can also result from slight changes in the initial specific activity of the repeatedly prepared isotope solutions. Figure 5 shows the reconstructed SPECT/CT images as well as the VOIs used in the adult kidney phantom of the Lu-177 experiment (a) as well as the corresponding spherical phantom of the I-131 experiment (b).

SPECT/CT Calibration for Different Isotopes

Table 3 shows the calibration factors determined from the enlarged VOIs for all kidneys (CF_K) and spheres (CF_S) as well as the average of all reference bottle calibration factors for all isotope solutions. Considerable deviations $\Delta_{K/S-Ref}$ of up to 9.8% to the attenuation-free reference can be observed with decreasing volume deviations. However, the percentage difference Δ_{S-K} between spherical and kidney phantoms of comparable volumes stays below 1.1% for all ages/volumes.

The applied enlargement factors $\Delta\rho$ as well as the radii $r_{N,S}/r_{VOI,S}$ and volumes $V_{VOI,S}/V_{VOI,K}$ are given in Table 4. Deviations from the ideal $\Delta\rho$ of the largest volume (adult column) can be attributed solely to inaccuracies in the VOI drawing. While only a quarter of a voxel has to be added to the radius in the Tc-99m acquisition, this factor increased to half a voxel for Lu-177 and even one voxel for I-131.

The graphical illustration of the calibration factors in Figure 6 illustrates the volume-dependent decrease in calibration factor, which is independent of the phantom geometry.

DISCUSSION

Assessment of the 3D Printing Technique

In this work, fused deposition modeling 3D printing was successfully used to manufacture a set of refillable, waterproof and chemically stable phantoms. With a maximum volumetric deviation of about 6% between the CAD model and the final 3D object even in case of the smallest kidney (volume ~ 9 mL), the printing accuracy is sufficient for SPECT/CT calibration measurements.

A large part of these deviations are caused by the major drawback of the single-extruder FDM 3D printing technique, namely the fact that horizontal layers or overhangs have to be underlaid by support material, making it necessary for many designs to be split in two parts, which are then separately printed (see Supplemental Figure 2b). As the seams have to be made thicker for a better adhesion of the epoxy adhesive, this can lead to volume differences between the initial design and the actually printed object. This problem could be addressed by upgrading the 3D printing system to dual extrusion, where a second extruder in combination with a second filament – typically with different chemical properties – is used to print support structures that can later be dissolved off the actual print. While polyvinyl acetate (PVA) – the most commonly used support material – is dissolvable in nothing but water, other filaments are dissolvable in more specific chemical solutions such as acetone (acrylonitrile butadiene styrene, ABS) or sodium hydroxide (polylactic acid, PLA). As alkaline solutions – such as the 1M NaOH used in case of the I-131 experiment in this work – are used for storage and transport of many radionuclides, PLA-based phantoms should always be coated with epoxy casting resin to prevent a potential decomposition. In combination with the high layer bonding of PLA-printed objects (tensile strength of ~ 57 MPa), the coating results in durable and chemically stable phantoms

(19). Despite minor differences between the designed models and the final printed objects, the presented setup – with sub-mm layer height and in-plane resolution – holds the potential for the design & fabrication of a wide range of anthropomorphic phantoms for SPECT/CT and PET/CT imaging systems with a resolution in the range of several millimeters. Moreover, the wide range of filaments available for FDM 3D printing with Hounsfield units from -60 to more than 3000 (18) enables the emulation of almost every tissue of interest.

As concluding remark, it should be noted that the size of objects to be 3D-printed is generally limited by the dimensions of the printer – in case of FDM the dimension of the printing bed in combination with the vertical printer dimension. Although these limitations are irrelevant for the kidney model of this study, they might be relevant if larger organs such as the liver or even whole-body models are to be printed (20).

SPECT/CT Calibration

Similar calibration factors were obtained for the attenuation-free reference and the largest phantoms (volume ~ 120 mL). The volume-dependent decrease can be explained by an increasing influence of partial-volume effects for small volumes.

The enlargement factors increasing from Tc-99m (LEHR collimator: $\langle \Delta\rho_{\text{Tc-99m}} \rangle = 0.25px = 1.2$ mm) and Lu-177 (MELP collimator: $\langle \Delta\rho_{\text{Lu-177}} \rangle = 0.52px = 2.5$ mm) to I-131 (high-energy collimator: $\langle \Delta\rho_{\text{I-131}} \rangle = 1.02px = 4.9$ mm) can be explained by the resolution of the collimators, which is deteriorating in this exact order. As the spatial resolution of the imaging system depends largely on the collimator, spill-out effects play the largest role for the high-energy collimator with the worst resolution. Although the enlarged VOIs represent a reasonable correction of

partial-volume effects for calibration measurements, care has to be taken in clinical settings when there is background activity and/or other structures in close vicinity to the target.

The difference in the VOI volumes of the kidney and the spherical phantoms can be explained by the type of VOI that was chosen in the analysis. While it is straightforward to draw an ellipsoidal VOI based on the diameter of the underlying sphere, it takes much more effort to draw a layer-by-layer polygon as it was done for the irregular shapes of the kidneys. The main problem is that the size of the smallest kidney dimension (newborn: $b_{\text{new}} = 9.3 \text{ mm}$) can be in the order of several voxels ($px = 4.8 \text{ mm}$), and small changes in the positioning of the phantom relative to the patient bed may considerably affect the volume needed to include all relevant counts in a CT-based VOI. Additionally, transitions between adjacent slices can cause problems in the VOI drawing: The inclusion of too many counts from one slice has to be compensated by including less counts in the adjacent slice to minimize potential errors (see red arrow in Figure 5a). For the above reasons, the volumes of all kidney VOIs were between 5% and 30% larger than the volumes of the corresponding spherical VOIs.

Although visually, less partial-volume errors seem to occur for the calibration factors of the kidney geometry in Figure 6 in comparison to the spheres, no relevant numerical differences were found (difference $< 1.1\%$).

Comparison to Previously Presented Clinical Prototyping

The use of phantoms for the development and testing of clinical imaging modalities is widely spread. Due to the non-availability of anthropomorphic phantoms, the majority of typically used phantoms consist of an arrangement of commercially available Lucite or silicone components

mimicking organ function or morphology without, however, accurately modeling the shape or the structure of the organs themselves (21).

Recently, the commercial availability of various 3D printing modalities has created the possibility of individually manufacturing phantoms for specific applications. In this context, commercially available phantoms reprinted using stereolithography (13) and multijet 3D printing (14) were shown to be functionally equivalent for SPECT and PET quality controls. Similarly, the polyjet 3D printing technique has been used for creating models with pathological entities to enhance the training experience of neurosurgeons (16) or develop patient-specific molecular imaging phantoms (15). These photopolymerization-based 3D printing techniques feature the highest resolution that is currently commercially available (600dpi × 600dpi in layers of 16-32 microns), in turn leading to a very smooth surface finish. In contrast, the lower resolving FDM technique (layer thickness down to ~ 100 microns) can produce visible layer lines on the side walls, resulting in a rough surface finish, which – in this work – was compensated by the coating. The major disadvantage of the photopolymerization-based techniques and at the same time the largest advantage of FDM printing is of financial nature. With a purchase price in the six-digit range, both the Objet 500 Connex as well as the Objet Eden 500V (Stratasys, Eden Prairie, MN) used in (15,16) by far exceed the lower four-digit price of the Renkforce RF1000 used in this work. The same applies for the Projet 3500 HD (3D Systems, Rock Hill, SC) that was used in (14) with a purchase price in the higher five-digit USD range. Together with a lower cost per printed volume, the FDM workflow presented in this work represents a serious low-cost alternative for manufacturing anthropomorphic or even patient-specific molecular imaging phantoms. This could facilitate the application of 3D printing for clinical prototyping even in small clinics and research sites.

Limitations and Improvement Possibilities of the One-compartment Kidney Model

The one-compartment, or equivalently, uniform-activity kidney phantom designed in this study mainly served the purpose of demonstrating the general feasibility of SPECT quantification based on FDM-printed, anthropomorphic phantoms. From the results of this work, it can be concluded that PLA-based FDM 3D printing along with the epoxy coating enables the production of chemically stable, fillable phantoms, which are sufficiently durable for SPECT/CT calibration studies. Although no significant differences in partial-volume effects were found between the kidney-shaped and the spherically-shaped one-compartment phantoms, this conclusion will have to be re-evaluated for more realistic kidney geometries, where a low-activity inner region is typically surrounded by a ring of higher activity (5).

In a next step, a medullary compartment could be added to the simplified kidney model of this work. The resulting two-compartment kidney phantom would be fillable with non-uniform distributions of activity and therefore enable a more realistic analysis of partial-volume effects typically occurring in kidneys.

Although an increasing number of production steps (e.g. coating and agglutination of individually printed parts) would have to be incorporated, the setup could eventually be used to produce structures of very high complexity – from multi-compartment MIRD organs to patient-specific organ models obtained from MRI- or CT-based image data.

CONCLUSION

The presented 3D printing setup holds the potential for the design and fabrication of a wide range of quasi-realistic anthropomorphic phantoms for test and validation of internal radiation dosimetry. Despite comparably low initial and material costs, FDM-based techniques still hold the potential for 3D printing objects with sub-mm resolution – an accuracy sufficient with respect to the resolution of clinically available SPECT/CT and PET/CT systems.

In a calibration study, quantitative SPECT/CT acquisitions showed no relevant differences between the calibration constants of uniform-activity kidney designs derived from MIRD pamphlet 19 (17) and the additionally manufactured reference spheres as they are typically used to determine SPECT/CT calibration factors (difference < 1.1%).

The setup could be used in the future for the improvement of internal radiation dosimetry by calibrating SPECT/CT imaging systems for different MIRD organs or more sophisticated and even patient-specific organ models. Similarly, height-specific calibration factors for planar imaging could be derived for various geometries using the height-adjustable attachment system.

In a next step, more complex structures such as a medullary compartment could be added to the simplified kidney model of this work. In this manner, organ-specific distributions of radionuclide-labeled peptides or metabolites could be examined more comprehensively.

Ultimately, affordable 3D printing techniques could be combined with patient-specific MRI or CT data to establish reliable and reproducible quantitative imaging for an individualized, patient-specific pre- or peri-therapeutic internal radiation dosimetry of the kidneys or other critical organs.

REFERENCES

1. Bodei L, Mueller-Brand J, Baum RP, et al. The joint IAEA, EANM, and SNMMI practical guidance on peptide receptor radionuclide therapy (PRRNT) in neuroendocrine tumours. *Eur J Nucl Med Mol Imaging*. 2013;40:800-816.
2. Lassmann M, Eberlein U. Radiation Dosimetry Aspects of (177)Lu. *Curr Radiopharm*. 2015;8:139-144.
3. Pfestroff A, Luster M, Jilg CA, et al. Current status and future perspectives of PSMA-targeted therapy in Europe: opportunity knocks. *Eur J Nucl Med Mol Imaging*. 2015;42:1971-1975.
4. Herrmann K, Schottelius M, Lapa C, et al. First-in-Human Experience of CXCR4-Directed Endoradiotherapy with ¹⁷⁷Lu- and ⁹⁰Y-Labeled Pentixather in Advanced-Stage Multiple Myeloma with Extensive Intra- and Extramedullary Disease. *J Nucl Med*. 2016;57:248-251.
5. Ljungberg M, Celler A, Konijnenberg MW, Eckerman KF, Dewaraja YK, Sjogreen-Gleisner K. MIRDO Pamphlet No. 26: Joint EANM/MIRD Guidelines for Quantitative ¹⁷⁷Lu SPECT Applied for Dosimetry of Radiopharmaceutical Therapy. *J Nucl Med*. 2016;57:151-162.
6. Dewaraja YK, Ljungberg M, Green AJ, et al. MIRDO pamphlet No. 24: Guidelines for quantitative ¹³¹I SPECT in dosimetry applications. *J Nucl Med*. 2013;54:2182-2188.
7. Dewaraja YK, Frey EC, Sgouros G, et al. MIRDO pamphlet No. 23: quantitative SPECT for patient-specific 3-dimensional dosimetry in internal radionuclide therapy. *J Nucl Med*. 2012;53:1310-1325.
8. Hull A. Stereolithography as a Tool for Prototype Molds. *Kunststoffe-German Plastics*. 1992;82:56-58.
9. Yan X, Gu P. A review of rapid prototyping technologies and systems. *Computer-Aided Design*. 1996;28:307-318.
10. Durham M. Rapid prototyping - Stereolithography, selective laser sintering, and polyjet. *Advanced Materials & Processes*. 2003;161:40-42.
11. Graves A. Stereolithography vs. PolyJet: Photopolymer 3D Printing Materials and Applications. *R&D Magazine*. 2016;58:14-17.
12. Miller MA, Hutchins GD. Development of anatomically realistic PET and PET/CT phantoms with rapid prototyping technology. Paper presented at: 2007 IEEE Nuclear Science Symposium Conference Record; Oct. 26 2007-Nov. 3 2007, 2007.
13. Hunt DC, Easton H, Caldwell CB. Design and construction of a quality control phantom for SPECT and PET imaging. *Med Phys*. 2009;36:5404-5411.

14. Bieniosek MF, Lee BJ, Levin CS. Technical Note: Characterization of custom 3D printed multimodality imaging phantoms. *Med Phys*. 2015;42:5913-5918.
15. Gear JJ, Long C, Rushforth D, Chittenden SJ, Cummings C, Flux GD. Development of patient-specific molecular imaging phantoms using a 3D printer. *Med Phys*. 2014;41:082502.
16. Waran V, Narayanan V, Karuppiyah R, Owen SL, Aziz T. Utility of multimaterial 3D printers in creating models with pathological entities to enhance the training experience of neurosurgeons. *J Neurosurg*. 2014;120:489-492.
17. Bouchet LG, Bolch WE, Blanco HP, et al. MIRD Pamphlet No 19: absorbed fractions and radionuclide S values for six age-dependent multiregion models of the kidney. *J Nucl Med*. 2003;44:1113-1147.
18. Lam K. MO-F-CAMPUS-I-03: CT and MR Characteristics of Some Specialty 3D Printing Filaments. *Med Phys*. 2015;42:3579-3579.
19. Tymrak BM, Kreiger M, Pearce JM. Mechanical properties of components fabricated with open-source 3-D printers under realistic environmental conditions. *Materials & Design*. 2014;58:242-246.
20. Rengier F, Mehndiratta A, von Tengg-Kobligk H, et al. 3D printing based on imaging data: review of medical applications. *Int J Comput Assist Radiol Surg*. 2010;5:335-341.
21. SabbirAhmed AS, Demir M, Kabasakal L, Uslu I. A dynamic renal phantom for nuclear medicine studies. *Med Phys*. 2005;32:530-538.

FIGURE CAPTIONS

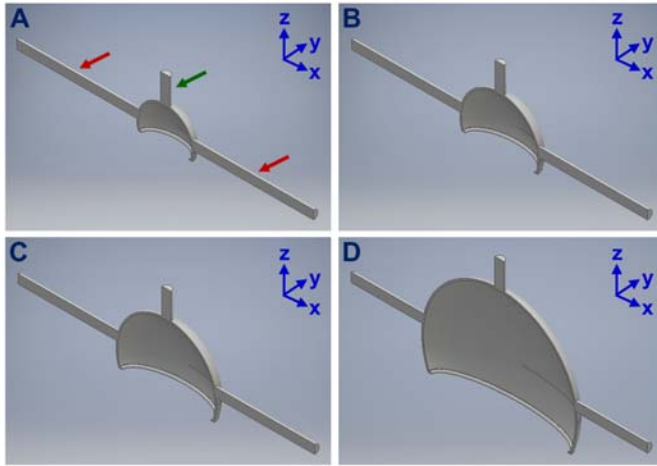


Figure 1: CAD models of the renal cortices. A: Newborn. B: 1-year-old. C: 5-year-old. D: Adult. Red arrows: Cylinders added for attachment. Green arrow: Cylinder added for filling.

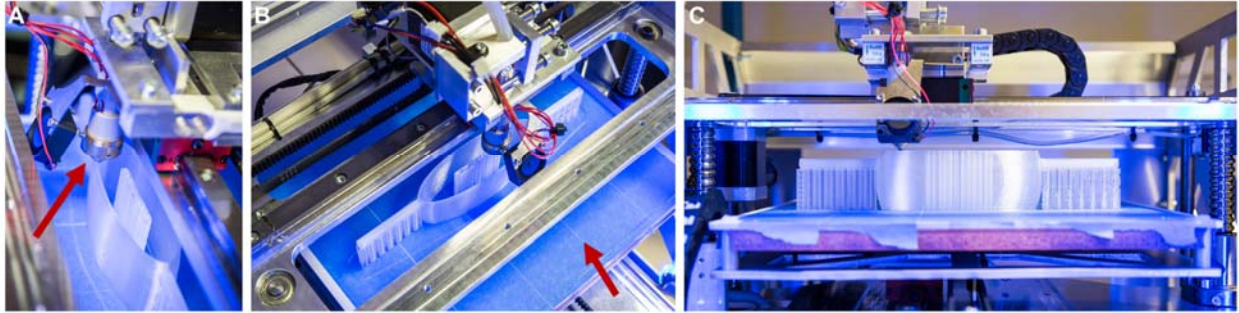


Figure 2: 3D printing process. A: Extruder. B: Movable printing plate. C: Profile.



Figure 3: Manufactured set of kidney phantoms. Smallest to largest: Newborn, 1-year-old, 5-year-old, adult.

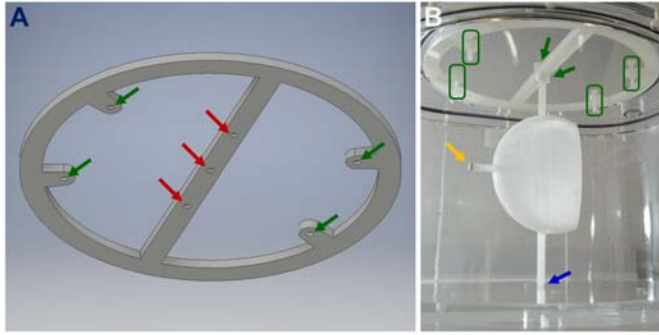


Figure 4: A: CAD design of the attachment system. Red arrows: Option for height adjustment of the kidneys. Green arrows: Holes for mounting spacers. B: Attachment of the kidney insert to the body phantom. Orange arrow: Sealing screw. Green arrows: Screw nuts for mounting the attachment system to the kidney insert. Green boxes: Spacers for fixing the position.

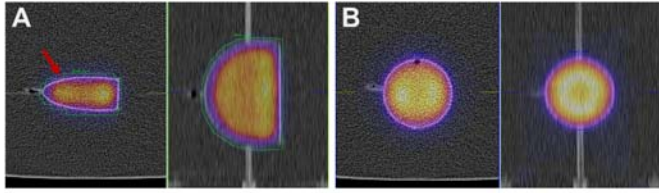


Figure 5: SPECT/CT reconstructions and VOIs used for determination of the calibration factors for the adult kidney filled with Lu-177 (A) as well as the adult sphere filled with I-131 (B).

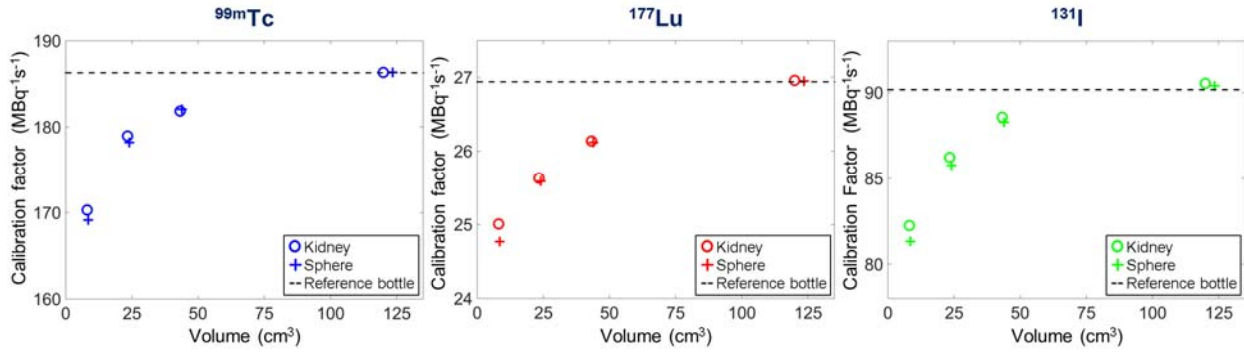


Figure 6: Volume-dependency of the calibration factors obtained in the kidneys (circles) and spheres (crosses) as well as the reference bottle (dotted line) filled with three different radionuclides.

TABLES

Table 1. Mathematical parameters of the old kidney model (MIRD19), the new kidney model, and the reference spheres for all different ages.

		Newborn	1 Year	5 Years	Adult
Kidney	a_{MIRD19} [mm]	17.9	26.1	32.0	45.0
	$b_{\text{MIRD19}} = b_{\text{new}}$ [mm]	9.3	12.5	14.0	15.0
	c_{MIRD19} [mm]	17.0	24.1	32.0	55.0
	$a_{\text{new}} = c_{\text{new}}$ [mm]	17.5	25.1	32.0	50.0
	d_{pelvis} [mm]	12.0	16.9	21.3	30.0
	V_{K} [cm ³]	8.59	24.15	44.36	122.93
Reference Sphere	r_{S} [mm]	12.7	17.9	22.0	30.8
	V_{S} [cm ³]	8.58	24.23	44.30	122.99

Table 2. Photo peak energy, lower scatter window and upper scatter window for all isotopes employed in this study.

	Photo Peak [keV]	Width [%]	Lower Scatter [%]	Upper Scatter [%]
Tc-99m	140	15	15	
Lu-177	208	20	10	10
I-131	364	15	15	15

Table 3. Calibration factors of kidneys (CF_K), spheres (CF_S) and the reference acquisition for all isotopes. Additionally, the percentage differences Δ_{S-Ref} and Δ_{K-Ref} to the attenuation-free reference are given. Δ_{S-K} stands for the deviation between CF_S and CF_K .

Isotope	VOI	Newborn	1 Year	5 Years	Adult	<Reference>
Tc-99m	CF_K [MBq ⁻¹ s ⁻¹]	170.32	178.97	181.83	186.32	186.29±2.26
	Δ_{K-Ref} [%]	8.6	3.9	2.4	0.018	
	CF_S [MBq ⁻¹ s ⁻¹]	169.16	178.2	182.06	186.34	
	Δ_{S-Ref} [%]	9.2	4.3	2.3	0.029	
	Δ_{S-K} [%]	0.69	0.43	0.13	0.011	
Lu-177	CF_K [MBq ⁻¹ s ⁻¹]	25.01	25.63	26.14	26.96	26.94±0.08
	Δ_{K-Ref} [%]	7.2	4.8	3.0	0.089	
	CF_S [MBq ⁻¹ s ⁻¹]	24.77	25.59	26.12	26.95	
	Δ_{S-Ref} [%]	8.0	5.0	3.0	0.068	
	Δ_{S-K} [%]	0.96	0.17	0.052	0.021	
I-131	CF_K [MBq ⁻¹ s ⁻¹]	82.24	86.22	88.57	90.54	90.17±0.59
	Δ_{K-Ref} [%]	8.8	4.4	1.8	0.41	
	CF_S [MBq ⁻¹ s ⁻¹]	81.33	85.76	88.28	90.40	
	Δ_{S-Ref} [%]	9.8	4.9	2.1	0.26	
	Δ_{S-K} [%]	1.1	0.53	0.33	0.16	

Table 4. Nominal ($r_{N,S}$) and VOI radii ($r_{VOI,S}$) as well as volumes ($V_{VOI,S}$, $V_{VOI,K}$) and enlargement factors $\Delta\rho_{\text{nuclide}}$ for a pixel size of 4.8 mm. Right column: Average over all ages for each isotope.

Isotope		Newborn	1 Year	5 Years	Adult	Average
	$r_{N,S}$ [cm]	1.27	1.80	2.20	3.09	
Tc-99m	$r_{VOI,S}$ [cm]	1.39	1.92	2.32	3.20	
	$\Delta\rho_{\text{Tc-99m}}$ [cm]	0.12	0.12	0.13	0.11	0.12±0.01
	$\Delta\rho_{\text{Tc-99m}}/px$	0.25	0.26	0.27	0.24	0.25±0.01
	$V_{VOI,S}$ [cm ³]	11.28	29.55	52.56	137.08	
	$V_{VOI,K}$ [cm ³]	12.99	33.61	58.27	161.38	
Lu-177	$r_{VOI,S}$ [cm]	1.54	2.04	2.44	3.33	
	$\Delta\rho_{\text{Lu-177}}$ [cm]	0.27	0.25	0.24	0.24	0.25±0.01
	$\Delta\rho_{\text{Lu-177}}/px$	0.56	0.52	0.50	0.50	0.52±0.03
	$V_{VOI,S}$ [cm ³]	15.25	35.75	60.53	153.98	
	$V_{VOI,K}$ [cm ³]	19.82	44.56	75.47	216.73	
I-131	$r_{VOI,S}$ [cm]	1.76	2.29	2.69	3.56	
	$\Delta\rho_{\text{I-131}}$ [cm]	0.49	0.49	0.49	0.47	0.49±0.01
	$\Delta\rho_{\text{I-131}}/px$	1.03	1.03	1.02	0.99	1.02±0.02
	$V_{VOI,S}$ [cm ³]	22.98	50.26	81.16	188.98	
	$V_{VOI,K}$ [cm ³]	27.56	55.86	97.47	229.38	